Energy Advances

ROYAL SOCIETY OF CHEMISTRY

PAPER

View Article Online
View Journal | View Issue

Cite this: *Energy Adv.*, 2025, 4, 1024

ORR durability study on $Pt_{3.7}Mn$/KB, $Pt_{3.9}Co$/KB and $Pt_{3.7}Ni$/KB for heavy-duty vehicle operation†

Galindev Oyunbileg,*[ab] Garavdorj Batnyagt,[a] Waka Nagano,[a] Hidenobu Wakita,[a] Koichi Ui[a] and Tatsuya Takeguchi*[a]

Received 4th March 2025,
Accepted 12th June 2025

DOI: 10.1039/d5ya00059a

rsc.li/energy-advances

Since durability is one of the key issues for using robust catalysts in fuel cell systems of heavy-duty vehicles (HDV, a durability target of 50 000 h) applications, the durability of various core–shell Pt-based alloy catalysts is evaluated. Herein, we present the durability behaviors of $Pt_{3.7}Mn$/KB (KB: EC600JD), $Pt_{3.9}Co$/KB and $Pt_{3.7}Ni$/KB catalysts with similar initial activities for the oxygen reduction reaction (ORR) of fuel cell systems. The durability of the catalysts was evaluated by a square-wave accelerated durability test (ADT) under the HDV operation. Notably, $Pt_{3.9}Co$/KB largely retained its mass activity (MA) even after 70 000 ADT cycles, while $Pt_{3.7}Mn$/KB and $Pt_{3.7}Ni$/KB significantly degraded during the tests. Less alteration in MA of $Pt_{3.9}Co$/KB was consistent with the slight change in the Tafel slope.

Introduction

Highly efficient and non-polluting polymer electrolyte fuel cells (PEFCs) aim to power HDVs which are significant sources of greenhouse gas emissions.[1–3] The United States Department of Energy (DOE) has set the 2025 targets for PEFC performance, a total loading of platinum group metal (PGM) and lifetime to achieve >0.3 A cm^{-2} at 0.8 V, 0.125 mg_{Pt} cm^{-2}, after ADT 5000-h for light-duty vehicles (LDVs), and 1.07 A cm^{-2} at 0.7 V, 0.3 mg_{Pt} cm^{-2}, after ADT 25 000-h for HDVs such as Class 8 long-haul trucks.[1,4] In addition, the Japanese New Energy & Industrial Development Organization (NEDO) has established more aggressive 2035 targets (0.761 V at 2.18 A cm^{-2}, 0.178 mg_{Pt} cm^{-2}, after ADT 50 000-h) for PEFC systems of HDVs.[5] These strict targets require usage of a highly active and robust catalyst for the cathodic reaction of PEFCs. A significant number of disordered and ordered Pt-based alloy catalysts with enhanced ORR activities have been extensively developed so far.[6–13] However, the insufficient durability still remains a critical challenge. In connection with the shift of PEFCs from LDV to HDV applications, state-of-the-art Pt-based catalysts have been evaluated for ORR durability under HDV operation conditions. For instance, a commercial Pt catalyst supported on a high surface area carbon (Pt/C) was evaluated and exhibited a high level of degradation.[14] Subsequently, the ORR durability of an ordered PtCo intermetallic catalyst ($L1_0$-PtCo/C) was examined with 90 000 ADT cycles and was about two times more stable than that of Pt/C.[15] The catalyst degradation is mainly caused by dissolution of Pt and secondary metals,[16,17] agglomeration of nanoparticles,[18,19] poisoning by sulfonic acid groups of ionomers[20,21] and corrosion of supports.[22] These detrimental processes are considerably decreased by protecting catalyst nanoparticles with specific shells. Shell-protection strategies used in catalyst preparation create shells composed of Pt atoms,[8,9] carbon cages[12,23,24] and oxide clusters[25,26] on the surface of alloy nanoparticles. Among them, the Pt-shell has a significant impact on the performance and durability of alloy-core/Pt-shell structured catalysts. This is because the Pt-shell protects secondary metal atoms from dissolution whereas the alloy-core enhances ORR activity by modifying the surface electronic structure of catalyst nanoparticles.[27] The core–shell structured alloy catalysts on carbon are often prepared by colloid,[28] impregnation,[29,30] polyol[31] and ball milling[32] strategies. However, the widely used colloid, polyol and ball milling methods suffer from incomplete removal of organic contaminants and inhomogeneous dispersion of metal precursors. In contrast, an aqueous solution-based impregnation (ASI) coupled with a rapid heating and quenching (RHQ) treatment is a clean method which can produce even a gram-scale catalyst for a short period of time. In addition, ASI provides homogeneous dispersion of metal precursors without organic contaminants on support, whereas RHQ not only prevents aggregation of nanoparticles by rapid-heating but also preserves defects on nanoparticle surfaces by rapid-cooling.[33] On the other hand, a robust catalyst is expected to have a larger average particle size to tolerate HDV PEFC operating conditions while maintaining its high ORR activity.[34] Herein, we prepared the core–shell structured alloy catalysts ($Pt_{3.7}Mn$/KB, $Pt_{3.9}Co$/KB and $Pt_{3.7}Ni$/KB) with well-controlled particle sizes (4–5 nm) using the

[a] *Faculty of Science and Engineering, Iwate University, Morioka, Iwate 020-8551, Japan. E-mail: takeguch@iwate-u.ac.jp*
[b] *Department of Chemistry, School of Arts and Science, National University of Mongolia, Ulaanbaatar 14201, Mongolia. E-mail: oyunbileg19@num.edu.mn*

† Electronic supplementary information (ESI) available. See DOI: https://doi.org/10.1039/d5ya00059a

ASI-RHQ method. The three alloy catalysts showed comparable initial ORR activities. However, their durability towards ORR was clearly differentiated by ADTs for 70 000 (70k) cycles. Notably, MA of $Pt_{3.9}Co$/KB was less altered by ADT experiments compared to $Pt_{3.7}Mn$/KB and $Pt_{3.7}Ni$/KB which significantly declined. The lower alteration in MA of $Pt_{3.9}Co$/KB correlated with negligible change in the Tafel slope.

Experimental

Chemicals

A ketjen-black carbon support (KB: EC-600JD, SA_{BET}: 1270 $m^2\ g^{-1}$)[35] was purchased from LION Specialty Chemicals. A commercial catalyst (cPt/C, 46.7 wt% Pt, $d_{TEM.}$: 2.3 nm) and a diaminedinitritoplatinum(II) aqueous solution (Pt 4.558 wt%, $[Pt(NH_3)_2](NO_2)_2$) were purchased from Tanaka Kikinzoku Kogyo (TKK). Cobalt(II) nitrate hexahydrate (CN, $Co(NO_3)_2{\cdot}6H_2O$, 98.0%), nickel(II) nitrate hexahydrate (NN, $Ni(NO_3)_2{\cdot}6H_2O$, 98.0%), manganese(II) nitrate hexahydrate (MN, $Mn(NO_3)_2{\cdot}6H_2O$, 98.0%), HNO_3 (60.0%), $HClO_4$ (70.0%), ethanol (99.5%), 1-propanol (infinity pure), a 5 wt% Nafion solution (DE520 CS), and ultrapure water (for LC/MS) were purchased from FUJIFILM Wako Pure Chemical Corporation. All chemicals were used as received.

Catalyst preparation

An aqueous suspension of KB (0.5 g), distilled water (80 mL) and ethanol (1 mL) was sonicated for 5 min and further stirred for 30 min at room temperature. Subsequently, an aqueous solution (10 mL) of diaminedinitritoplatinum(II) solution (Pt: 0.0026 mol) and transition-metal (M) nitrate (M: 0.0012 mol) was added dropwise to the suspension. The resultant mixture was stirred at room temperature for 2 h, vacuum-distilled at 65 °C to remove the solvent, and dried in air at 50 °C overnight. The dry solid was decomposed at 200 °C (a ramping rate of 3 °C min^{-1}) for 2 h under a nitrogen atmosphere and reduced at 100 °C (2.5 °C min^{-1}) and 150 °C (2 °C min^{-1}), respectively, for 30 min under a 5% H_2/Ar flow. Subsequently, the powder was exposed to RHQ treatment. In other words, it was rapidly heated to 880 °C within 2 min, maintained at 880 °C for 1 h under the 5% H_2/Ar atmosphere and rapidly cooled using a fan to room temperature within 15 min to obtain alloy nanoparticles. Then, the alloy catalyst was treated with 1.0 M HNO_3 at 80 °C for 12 h, vacuum-filtered, rinsed with distilled water (1000 mL) and dried in air at room temperature overnight. The obtained core–shell structured alloy catalyst was dried at 80 °C for 10 h under nitrogen, followed by post-heat treatment at 500 °C under the 5% H_2/Ar atmosphere for a short period of time. In all cases, the gas flow rate was set at 60 mL min^{-1}.

Characterization

The X-ray diffraction (XRD) patterns were recorded from 10° to 90° 2θ angles at a scanning rate of 2° min^{-1} and a step of 0.02° on a MiniFlex 600-C diffractometer (Rigaku) using a CuKα radiation (λ = 1.541862 Å) at 40 kV and 15 mA. Transmission electron microscopy (TEM) images were taken at 200 kV with a JEM-2100 electron microscope (JEOL Ltd.). The metal loadings were estimated by calcination in air followed by reduction in 5%H_2/Ar on a Seiko SII-EXSTAR TG/TDA-7200 analyser (Nanotechnology Inc.). The metal ratios were determined using a NEX DE X-ray fluorescence (XRF) system (Rigaku). X-ray photoelectron spectroscopy (XPS) scans were performed on a PHI 5000 VersaProbe (ULVAC-PHI, Inc.) using a monochromatic Al Kα X-ray source (1486.6 eV) at 25 W (15 kV, 3 mA). The XPS survey spectra were collected with a pass energy of 187.85 eV in the binding energy (BE) range of 0–1000 eV with a step of 1.0 eV and a dwell time of 20 ms. The core level (narrow) spectra were scanned with a pass energy of 23.5 eV at a step of 0.1 eV and a dwell time of 50 ms. The atomic fraction of $M(x)$ in alloy nanoparticles was determined from XRD data based on Vegard's law (eqn (1)).[36]

$$a_{alloy} = a_M x + a_{Pt}(1 - x) \quad (1)$$

where a_{alloy}, a_M and a_{Pt} are lattice parameters of experimentally prepared alloy catalyst, bulk M and bulk Pt, respectively.

Electrochemical measurements

Electrochemical measurements were performed using a potentiostat (VSP-300, Bio-Logic SAS), an electrode rotator (AFMSRCE, Pine Research Instruments), and a three-electrode electrochemical cell (Pine Research Instruments). A glassy carbon (GC, 0.196 cm^2 area, Pine Research Instruments) polished with 0.05 μm alumina slurry was used as a working electrode support. A platinum coil electrode (BAS Inc.) and a reversible hydrogen electrode with a double junction chamber (RHE, BAS Inc.) were employed as a counter electrode (CE) and a reference electrode (RE), respectively. All potential values are referred to RHE and *iR*-corrected ($E_{iR\text{-free}} = E_{meas.} + iR_s$) after each measurement. A catalyst ink composed of catalyst powder, ultrapure water, and 5 wt% Nafion solution was ultrasonically dispersed in an ice-cooled bath for 1 h, followed by horn sonication (15 W, 60 s).[37] The ratios of water : 1-propanol and ionomer : carbon (I/C) were 1 : 3 and 1 : 2, respectively. The Pt loading was 18 $\mu g_{Pt}\ cm^{-2}$. A 10 μL of the catalyst ink was applied on a pre-polished GC tip mounted on an inverted rotator shaft while spinning at 100 rpm and the solvent was dried at 700 rpm in ambient air. The working electrode with a catalyst layer was immersed in 0.1 M $HClO_4$ solution (~130 mL). After the electrolyte was purged with nitrogen (300 mL min^{-1}) for 30 min, the working electrode was scanned at 200 mV s^{-1} from 0.0 to 1.1 V for 100 cycles to obtain stable and clean surface. Last three cyclic voltammograms (CVs) were recorded at 50 mV s^{-1} from 0.02 to 0.5 V for the calculation of electrochemical surface areas (ECSAs). ECSAs were estimated from the hydrogen adsorption charge (Q_H) between 0.05 and 0.40 V after double-layer correction (eqn (2)).

$$\text{ESCA}\ (m_{Pt}^2\ g^{-1}) = Q_H/(2.10 \times Pt_{loading}) \quad (2)$$

where 2.10 (C m_{Pt}^{-2}) is the electric charge for a monolayer hydrogen on Pt surface and $Pt_{loading}$ (g) is the Pt mass. The solution resistance (R_s = ~25 Ω) was measured at 0.5 V with an amplitude of 0.015 V in the frequency range of 100 000 Hz to 1 Hz. Subsequently, linear sweep voltammograms (LSVs) were

measured at 10 mV s^{-1} from 0.3 V to 1.1 V to record the background currents. After that, the electrolyte was purged with oxygen (300 mL min^{-1}) for 30 min while measuring the open circuit voltage (OCV). LSVs for ORR were scanned at 10 mV s^{-1} from 0.3 to 1.1 V at rotation speeds of 200, 400, 900, 1600 and 2000 rpm in the O_2-saturated electrolyte at room temperature. The kinetic currents (i_k) at various potentials were calculated from LSV curves using the Koutecky–Levich formula (eqn (3)).[38]

$$i_m^{-1} = i_k^{-1} + i_L^{-1} \quad (3)$$

where i_m is the measured current, i_k is the kinetic current and i_L is the diffusion-limited current at 0.4 V. The i_k obtained from the intercept of the Koutecky–Levich linear plot at 0.9 V was normalized with Pt loading and ECSA to evaluate the MA and specific activity (SA), respectively, according to eqn (4) and eqn (5).

$$\text{MA (A } g_{Pt}^{-1}) = i_k/Pt_{loading} \quad (4)$$

$$\text{SA } (\mu A\ cm_{Pt}^{-2}) = i_k/\text{ECSA} \quad (5)$$

In addition, Tafel slopes were extracted from the plots of $E_{iR\text{-free}}$ against log(i_k) at low current regions. The square-wave ADTs were performed using constant potential polarization at 0.6 V (3 s) and 0.95 V (3 s) for 70k cycles in the N_2-saturated 0.1 M $HClO_4$ at room temperature (25 °C ± 3 °C).[39] At the beginning of ADT and after every 10 000 (10k) cycles, CVs and LSVs were measured in the N_2- and O_2-saturated fresh electrolyte, respectively, to evaluate ECSAs and ORR activities. Single cell tests were performed according to a protocol recommended by NEDO.[40] The catalyst ink composed of catalyst powder, ultrapure water, ethanol and 5 wt% Nafion solution was ultrasonically dispersed in an ice-bath for 1 h. The ratios of water: ethanol and I/C were 2 : 3 and 1 : 1, respectively. The anode/cathode Pt loadings were fixed at 0.17 mg_{Pt} cm^{-2}/0.17 mg_{Pt} cm^{-2}. The anode (cPt/C, 46.7 wt% Pt, TKK) and cathode (alloy catalyst) electrodes were produced by painting the catalyst inks on carbon papers (MB30, Avcarb). A membrane electrode assembly (MEA, 1 cm^2) was fabricated by hot-pressing a proton-exchange membrane (NRE211 Nafion membrane, Chemours) between the anode and cathode electrodes with a force of 2 MPa at 135 °C for 20 min. The MEA was assembled into a single cell and connected to fuel cell testing systems (FC5100 and DB630, Chino, Japan). During *I–V* measurements, the single cell was operated at 80 °C, and the anode and cathode humidifiers were set at 73 °C. The relative humidity (RH) of inlet gases was maintained at 75%. The hydrogen (418 mL min^{-1}) and air (998 mL min^{-1}) pressurized at 50 kPa-G were supplied to the anode and cathode components, respectively. The *I–V* polarization curves were recorded starting from the low-current region, at current densities of 2, 4, 6, 10, 20, 50, 75, 100, 200, 400, 600, 800, 1000, 1500, 2000 mA cm^{-2} while measuring for 10 min at each current density.

Results and discussion

Catalyst preparation

In this study, the core–shell structured alloy catalysts ($Pt_{3.7}Mn$/KB, $Pt_{3.9}Co$/KB and $Pt_{3.7}Ni$/KB) were prepared by the ASI-RHQ method according to the scheme shown in Fig. 1. The method consists of five main steps such as impregnation, decomposition-reduction (DR), RHQ, acid-treatment, and post heat-treatment (post-HT), as described in ESI.† The impregnation anchors metal precursors to the KB support while producing their highly homogenous dispersion in an aqueous solution without organic impurities. The DR step sequentially converts the anchored precursors to solid intermediates, which may be partially reduced oxides, *via* dehydration, decomposition and mild reduction processes. Notably, no oxide phases (Co_3O_4, CoO, MnO_2, MnO, NiO, *etc.*) were detected in the XRD spectra of solid materials after DR (Fig. S1, ESI†). However, they may exist as amorphous phases. The RHQ step transforms the partially reduced solids into alloy nanoparticles at a high temperature under a reducing condition. The acid-treatment removes M species from the surface of alloy nanoparticles to build the Pt-shell, while the post-HT rearranges Pt atoms at the shell surface. For the alloy catalysts, the Pt : M ratios determined by XRD were essentially identical to the ratios estimated from XRF. This reflected the ASI-RHQ enabling us to obtain well-dissolved solid phases from a highly homogenous dispersion of metal precursors on KB. Previously, the preparation condition of the RHQ method was examined for various Pt–Ru catalysts with the ratio of $n_{Pt-Ru}/(n_{Pt-Ru} + n_{Pt-Pt})$ which was precisely determined by EXAFS using the BL36XU beamline of SPring-8 (Proposals 2017B7901 and 2018A7901).[41] Subsequently, this method was expanded to the preparation of Pt-M catalysts.

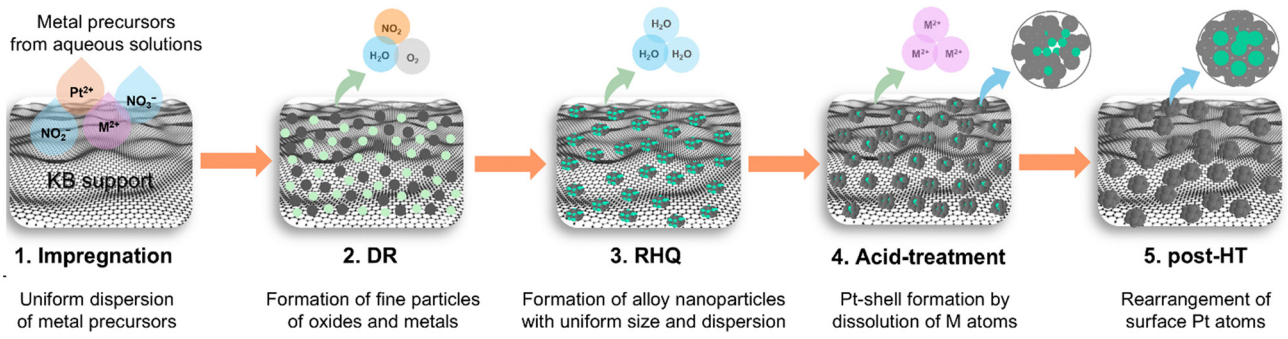

Fig. 1 A general scheme for the ASI-RHQ preparation method of the core–shell structured alloy catalysts.

Characterization

XRD patterns of alloy catalysts ($Pt_{3.7}Mn$/KB, $Pt_{3.9}Co$/KB and $Pt_{3.7}Ni$/KB) and cPt/C are shown in Fig. 2. Both $Pt_{3.9}Co$/KB (PDF#01-072-9178) and $Pt_{3.7}Ni$/KB similar to cPt/C (Pt: PDF#00-004-0802) provide the characteristic diffraction peaks from a disordered face-centred cubic (fcc) structure with a $Fm\bar{3}m$ space group.[6,11] On the contrary, the $Pt_{3.7}Mn$/KB (PDF#01-071-9674) exists as an ordered phase which was identified by the additional peaks at 2θ angles of 22.81°, 32.42°, 52.49°, 57.96°, 72.74° and 77.43°.[42] Also, $Pt_{3.7}Mn$/KB has the fcc structure with a $Pm\bar{3}m$ space group which was confirmed by matching the *d*-spacings of all the observed peaks.

A broad 002 peak at *ca.* 25° is assigned to the KB support. In addition, the diffraction peaks of the alloy catalysts shifted to wider 2θ angles than those of cPt/C, indicating formation of alloy nanoparticles. The shift was smaller for $Pt_{3.7}Mn$/KB with larger Mn (137 pm) atoms, while it was larger for $Pt_{3.9}Co$/KB and $Pt_{3.7}Ni$/KB containing smaller Co (125 pm) and Ni (125 pm) atoms, respectively.[43] On the other hand, XRD patterns after DR, RHQ and post-HT for each alloy catalyst are compared in Fig. S1 (ESI†). Using them, we examined shifts in the diffraction peaks after RHQ and post-HT to confirm the Pt-shell formation. The peaks shifted positively after RHQ whereas they shifted negatively after post-HT following the acid treatment. For example, a smaller shift in the $2\theta_{(220)}$ angle (RHQ → post-HT) was extracted for $Pt_{3.7}Mn$/KB (68.01° → 67.93°), $Pt_{3.9}Co$/KB (69.34° → 69.17°) and $Pt_{3.7}Ni$/KB (69.42° → 69.34°). These shifts indicate that dissolution of the surface M species leads

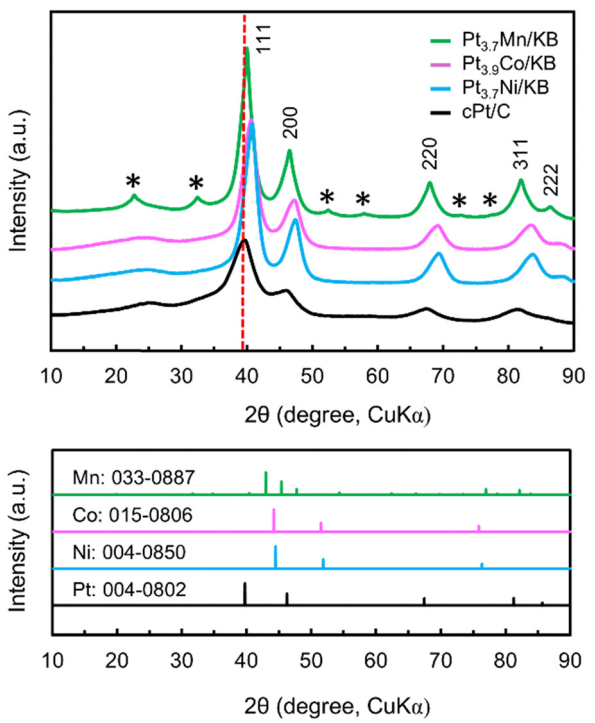

Fig. 2 The XRD patterns of $Pt_{3.7}Mn$/KB, $Pt_{3.9}Co$/KB, $Pt_{3.7}Ni$/KB and cPt/C. Asterisks indicate the ordered phase of $Pt_{3.7}Mn$/KB. The reference diffraction peak positions of bulk Mn, Co, Ni and Pt are also shown below.

Table 1 Physical properties of the prepared alloy catalysts

Catalyst (Pt_nM/KB)	Composition (wt%)	Structure
$Pt_{3.7}Mn$/KB	Pt: 50.1%, Mn: 3.8%	Ord. fcc
$Pt_{3.9}Co$/KB	Pt: 48.3%, Co: 3.8%	Dis. fcc
$Pt_{3.7}Ni$/KB	Pt: 49.0%, Ni: 4.0%	Dis. fcc

to formation of the Pt-shell. The physical properties such as metal compositions, crystalline structures and particle sizes of the alloy catalysts are summarized in Table 1.

The Pt_nM ($x_{total} = 1/(n_{total} + 1)$) ratios were estimated from XRF results. TG analysis provided a total metal content of 53.9%, 52.1% and 53.0% for $Pt_{3.7}Mn$/KB, $Pt_{3.9}Co$/KB and $Pt_{3.7}Ni$/KB, respectively. Based on TG and XRF results, the Pt and M contents in each catalyst were determined, respectively, as given in Table 1. Fig. 3A–C present TEM images of spherically shaped alloy nanoparticles in the prepared catalysts. The average particle sizes (d_{TEM}) estimated from *ca.* 300 nanoparticles in each catalyst were within the range of 4.2–4.6 nm which are about two times larger than that of cPt/C (2.3 nm). A small number of nanoparticles which were smaller and larger than average also exist in each catalyst.

We believe that the larger particle sizes of the alloy catalysts have a favourable impact on the lifetime of PEFCs for HDVs. In Fig. 3D–F, the particle size distribution histograms of the alloy catalysts exhibit a narrow distribution, suggesting that the particle sizes were controlled by the RHQ process. Also, TEM images reveal an even dispersion of less agglomerated alloy nanoparticles on the support material, showing potential benefits of the ASI-RHQ preparation method. The XPS analysis was performed to investigate the electronic structure of the surface species of the alloy catalysts before ADT. In the XPS survey spectrum of each catalyst, the signals for Pt, C and O were clearly detected, while the signals for M species were hardly observed which confirms the Pt-shell covers the alloy nanoparticles (Fig. S2, ESI†). In the narrow spectra shown in Fig. 4, the Pt 4f doublets of each catalyst were deconvoluted into the metallic (Pt^0) and oxidized (Pt^{2+} and Pt^{4+}) states.[44] The Pt^{2+} state corresponds to PtO and $Pt(OH)_2$, whereas the Pt^{4+} state correlates with PtO_2. The XPS quantitative analysis showed that the chemical states of Pt were identical on the surfaces of all alloy catalysts. It implies that the surface electronic structure of these alloy catalysts is independent of the M metal species.

Electrocatalytic activity before and after ADT

ORR activities of $Pt_{3.7}Mn$/KB, $Pt_{3.9}Co$/KB and $Pt_{3.7}Ni$/KB were evaluated on working electrodes with a catalyst layer ($Pt_{loading}$: 18 μg_{Pt} cm^{-2} and I/C: 0.5) by a rotating disk electrode (RDE). For comparative studies, the benchmark cPt/C was also studied under the same conditions. The CV curves obtained in N_2-saturated 0.1 M $HClO_4$ electrolyte before (initial) and after ADT (70k) are shown in Fig. 5A and B. The initial ECSA values were lower for $Pt_{3.7}Mn$/KB (56.83 m^2 g_{Pt}^{-1}), $Pt_{3.9}Co$/KB (60.27 m^2 g_{Pt}^{-1}) and $Pt_{3.7}Ni$/KB (51.08 m^2 g_{Pt}^{-1}) than cPt/C (78.06 m^2 g_{Pt}^{-1}) because of their larger particle sizes (4.2–4.6 nm) and modified surface electronic structures. The LSV curves measured at 1600 rpm in O_2-saturated 0.1 M $HClO_4$ before and after ADT (70k) are shown

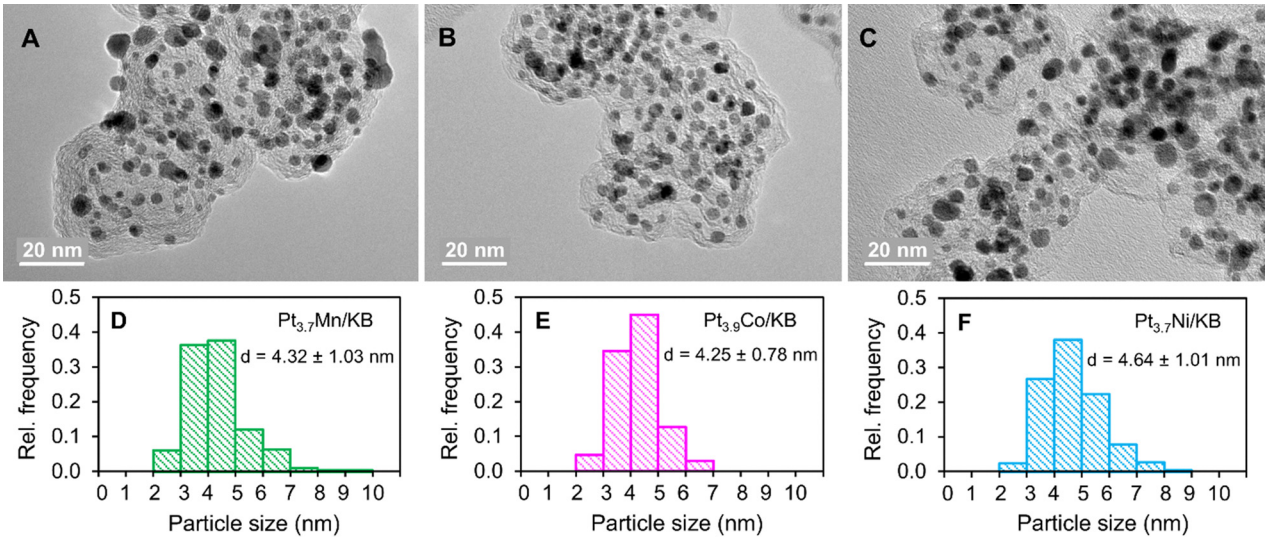

Fig. 3 (A)–(C) TEM images and (D)–(F) particle size distribution histograms of $Pt_{3.7}Mn/KB$ (A) and (D), $Pt_{3.9}Co/KB$ (B) and (E) and $Pt_{3.7}Ni/KB$ (C) and (F) alloy catalysts.

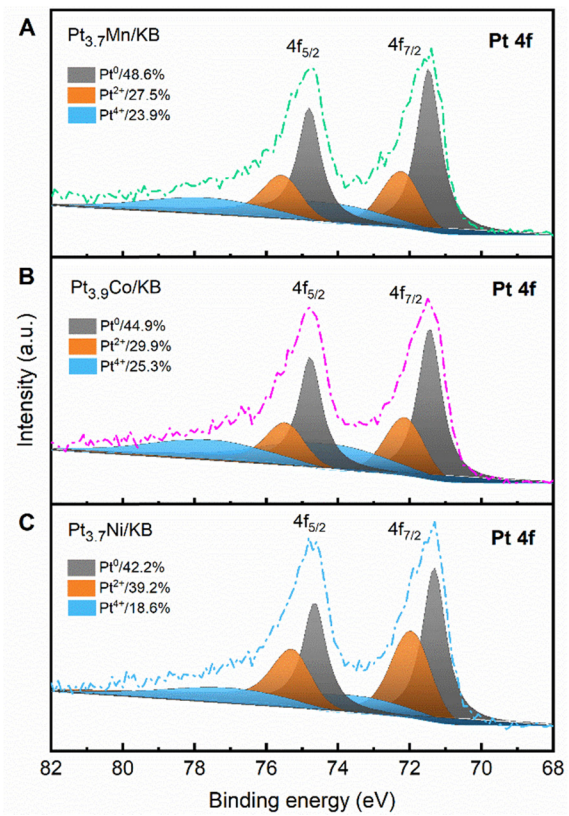

Fig. 4 The Pt 4f XPS spectra of (A) $Pt_{3.7}Mn/KB$, (B) $Pt_{3.9}Co/KB$ and (C) $Pt_{3.7}Ni/KB$ catalysts before ADT.

in Fig. 5C and D. The initial half-wave potential ($E_{1/2}$) of the prepared alloy catalysts was more positive by 16–22 mV than that of cPt/C, indicating their high intrinsic ORR activity. The high ORR activity of alloy catalysts stems from the modified electronic structure of surface Pt atoms owing to ligand, strain and ensemble effects induced by M atoms in alloy nanoparticles.[45] Kinetic current densities are compared in the Tafel plots at low current density regions. In Fig. 5E, the initial Tafel slopes were 72.39, 70.30, 71.54 and 65.47 mV dec^{-1} for $Pt_{3.7}Mn/KB$, $Pt_{3.9}Co/KB$, $Pt_{3.7}Ni/KB$, and cPt/C, respectively. As shown in Fig. 5F, the Tafel slopes of the alloy catalysts not only increased but also differentiated from each other after ADT (70k). It shows the changes in their surface chemical states which were initially identical according to the XPS analysis. Among them, $Pt_{3.9}Co/KB$ exhibited the smallest change in its Tafel slope, indicating its stable surface states. The initial SA of $Pt_{3.7}Mn/KB$, $Pt_{3.9}Co/KB$ and $Pt_{3.7}Ni/KB$ catalysts was 708, 978 and 1081 μA cm_{Pt}^{-2}, respectively, which are 1.6–2.2 times higher than that of cPt/C (439 μA cm_{Pt}^{-2}). In addition, the initial MA of $Pt_{3.9}Co/KB$ (589 A g_{Pt}^{-1}), $Pt_{3.7}Ni/KB$ (552 A g_{Pt}^{-1}) and $Pt_{3.7}Mn/KB$ (472 A g_{Pt}^{-1}) was 1.4–1.7 times higher than that of cPt/C (342 A g_{Pt}^{-1}), reflecting their superior ORR activity over that of pure Pt catalysts. The initial activities of the alloy catalysts are comparable, suggesting that catalytic activity is largely independent of the specific alloying metal. This may be attributed to the Pt-shell structures of the alloy catalysts having essentially equivalent surface electronic properties.[8] MAs of the alloy catalysts before and after ADT (70k) were compared in Fig. 6A. A relatively low decline in MA was observed for the alloy catalysts tested in this study compared to other studies.[12,46] The enhanced durability is attributed not only to the Pt-shell, which inhibits the dissolution of M atoms from the alloy catalysts, but also to the low amount of M atoms present.[47–49] In addition to the catalyst characteristics, it might depend on the experimental conditions such as temperature, loading amount and cleanliness of the cell as well as glassware. We thoroughly rinsed the catalyst layer on a GC tip with a fresh electrolyte after every ADT experiment and before each electrochemical measurement. Notably, the lowest loss in MA was observed for the $Pt_{3.9}Co/KB$ (1.7%) compared to $Pt_{3.7}Mn/KB$ (6.4%) and $Pt_{3.7}Ni/KB$ (6.0%) after ADT (70k), indicating its high durability toward ORR. We also examined the practical cell performance of $Pt_{3.9}Co/KB$ under MEA

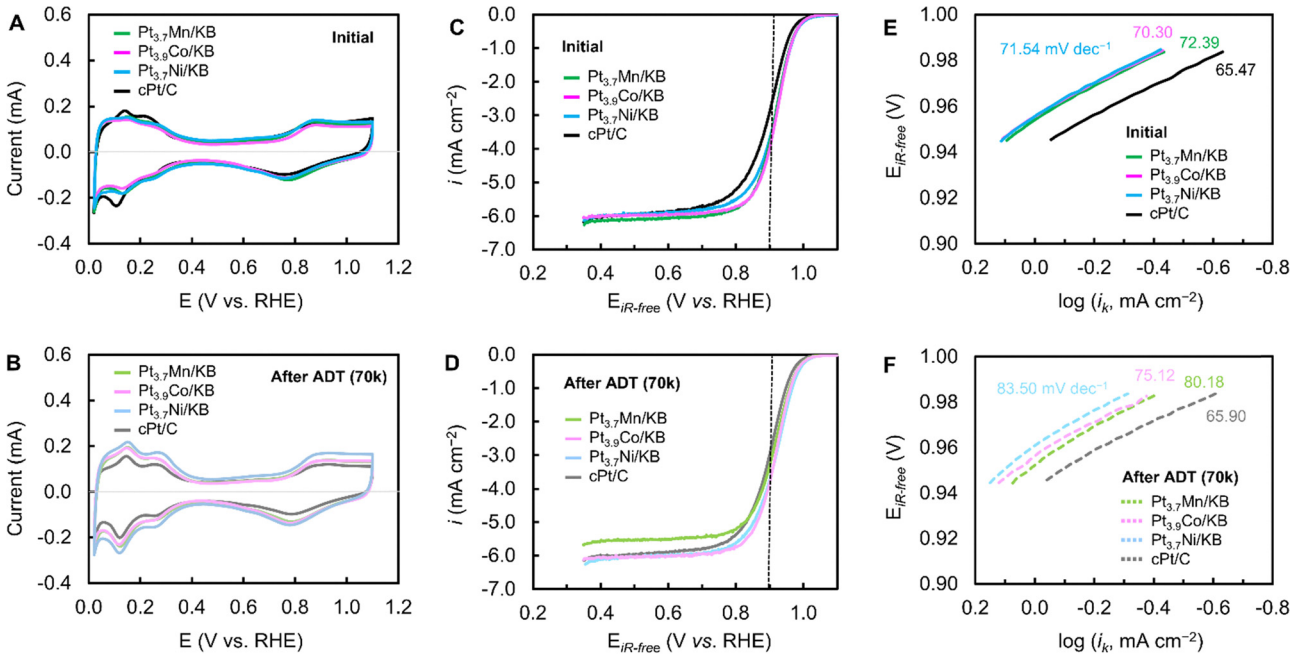

Fig. 5 The CVs (A) and (B), LSVs (C) and (D) and Tafel slopes (E) and (F) of $Pt_{3.7}Mn/KB$, $Pt_{3.9}Co/KB$ and $Pt_{3.7}Ni/KB$ along with cPt/C before (A), (C) and (E) and after (B), (D) and (F) ADT (70k). CVs (at 0 rpm) and LSVs (at 1600 rpm) were measured in the N_2- and O_2-saturated 0.1 M $HClO_4$ electrolyte, respectively. The Tafel slopes were estimated from the kinetic currents at 0.945–0.983 V.

operation conditions to confirm its ORR activity obtained by RDE. The *I–V* polarization curves were measured on the single cell assembled from MEA (1 cm^2), anode (cPt/C, Pt loading: 0.17 mg cm^{-2}) and cathode ($Pt_{3.9}Co/KB$, Pt loading: 0.17 mg cm^{-2}) electrodes. The measurements were performed at 80 °C and 75% RH, using hydrogen as a fuel and air as an oxidant, under a 50 kPa-G pressure. For comparison, cPt/C was also tested as the cathode catalyst. As shown in Fig. 6B, the $Pt_{3.9}Co/KB$ showed high performances at 0.2 A cm^{-2} (0.773 V) and at 1.0 A cm^{-2} (0.697 V) compared to the cPt/C (0.761 V at 0.2 A cm^{-2} and 0.656 V at 1.0 A cm^{-2}), confirming its high intrinsic activity toward ORR. Additionally, the initial cell performances of $Pt_{3.9}Co/KB$ (ASI-RHQ) and $Pt_{3.6}Co/KB$ (conventional method), prepared using two different approaches, are compared in Fig. S3 (ESI†). The high activity of $Pt_{3.9}Co/KB$ is attributed to ASI-RHQ, which yields homogeneously distributed alloy nanoparticles with relatively uniform sizes. In contrast, the conventional method results in non-uniform particle sizes and greater agglomeration. Briefly, the conventional method consisted of the following steps: (1) formation of Pt nanoparticles on the KB support, (2) precipitation of a cobalt precursor, (3) reduction under a reducing atmosphere, (4) acid-treatment and (5) post-HT. On the other hand, ADT tests on the commercial catalyst (cPt/C) were conducted at 80 °C and 75% RH, using hydrogen as the fuel and air as the oxidant, without back pressure. As shown in Fig. S4 (ESI†), cPt/C exhibited an ECSA loss of nearly 50%, decreasing from 54.6 to 26.1 m^2 g_{Pt}^{-1} after 30 000 ADT cycles. Based on this result, the durability results observed at 25 °C are considered reasonable.

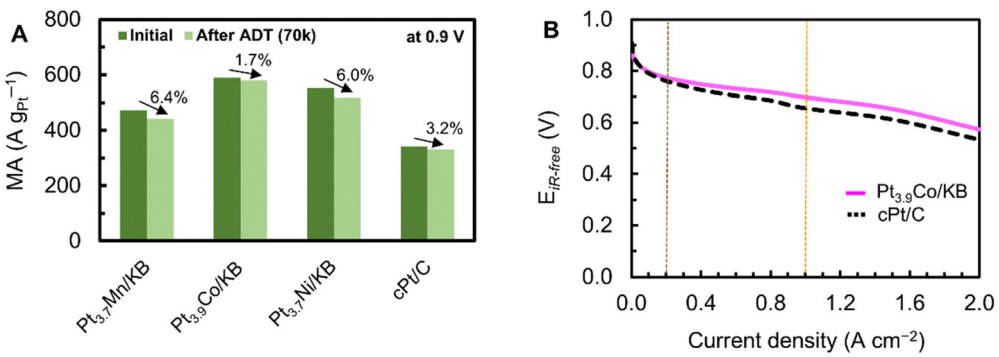

Fig. 6 (A) MAs at 0.9 V before (initial) and after ADT (70k) of $Pt_{3.7}Mn/KB$, $Pt_{3.9}Co/KB$, $Pt_{3.7}Ni/KB$ and cPt/C in O_2-saturated 0.1 M $HClO_4$. (B) *I–V* polarization curves of $Pt_{3.9}Co/KB$ and cPt/C measured at 80 °C, 75% RH, H_2/Air 50 kPa-G.

Conclusion

In this study, we evaluated the durability of the core–shell structured $Pt_{3.7}Mn$/KB, $Pt_{3.9}Co$/KB and $Pt_{3.7}Ni$/KB catalysts by ADT for 70 000 cycles under HDV operation conditions. The alloy catalysts having similar metallic composition, particle size and surface state showed comparable initial activities towards ORR. However, their durability was quite different by ADT evaluation. In comparison to $Pt_{3.7}Mn$/KB and $Pt_{3.7}Ni$/KB, the $Pt_{3.9}Co$/KB well-maintained its MA after ADT (70k), associating with slight variation in the Tafel slope. Therefore, the present study results suggest that the core–shell Pt_nCo-based alloy catalysts could be key candidates for durable PEFC systems in HDV applications.

Author contributions

G. O. performed synthesis, electrochemical measurement, data curation, formal analysis and manuscript preparation. G. B. and W. N. performed *I–V* measurements and took TEM images. H. W., K. U. and T. T. provided experimental supervision, data validation and review processes. All authors reviewed the manuscript.

Conflicts of interest

There are no conflicts to declare.

Data availability

The data supporting this article have been included as part of the ESI.†

Acknowledgements

This work was supported by a grant from New Energy and Industrial Technology Development Organization (NEDO), Japan.

References

1 D. A. Cullen, K. C. Neyerlin, R. K. Ahluwalia, R. Mukundan, K. L. More, R. L. Borup, A. Z. Weber, D. J. Myers and A. Kusoglu, *Nat. Energy*, 2021, **6**, 462.
2 M. De Las, N. Camacho, D. Jurburg and M. Tanco, *Int. J. Hydrogen Energy*, 2022, **47**, 29505.
3 S. Li, N. Gjilali, M. A. Rosen, C. Crawford and P.-C. Sui, *Int. J. Energy Res.*, 2022, **46**, 11718.
4 G. Yang, C.-H. Lee, X. Qiao, S. K. Babu, U. Martinez and J. S. Spendelow, *Electrochem. Energy Rev.*, 2024, **7**, 9.
5 Fuel Cell and Hydrogen Technology Roadmap: Fuel Cell Roadmap for FCVs/HDVs, NEDO, **https://www.nedo.go.jp/content/800020391.pdf**.
6 J. Greeley, I. E. L. Stephens, A. S. Bondarenko, T. P. Johansson, H. A. Hansen, T. F. Jaramillo, J. Rossmeisl, I. Chorkendorff and J. K. Nørskov, *Nat. Chem.*, 2009, **1**, 552.
7 C. Lim, A. R. Fairhurst, B. J. Ransom, D. Haering and V. R. Stamenković, *ACS Catal.*, 2023, **13**, 14874.
8 V. R. Stamenković, B. S. Mun, K. J. J. Mayrhofer, P. N. Ross and N. M. Marković, *J. Am. Chem. Soc.*, 2006, **128**, 8813.
9 C. Wang, M. Chi, D. Li, D. Strmcnik, D. van der Vliet, G. Wang, V. Komanicky, K.-C. Chang, A. P. Paulikas, D. Tripkovic, J. Pearson, K. L. More, N. M. Marković and V. R. Stamenković, *J. Am. Chem. Soc.*, 2011, **133**, 14396.
10 V. R. Stamenković, T. J. Schmidt, P. N. Ross and N. M. Marković, *J. Phys. Chem. B*, 2002, **106**, 11970.
11 H. Yano, I. Arima, M. Watanabe, A. Iiyama and H. Uchida, *J. Electrochem. Soc.*, 2017, **164**, F966.
12 Y. Gao, T. Uchiyama, K. Yamamoto, T. Watanabe, S. Tominaka, N. Thakur, R. Sato, T. Teranishi, H. Imai, Y. Sakurai and Y. Uchimoto, *ACS Catal.*, 2023, **13**, 10988.
13 M. Song, F. Li, Q. Zhang, T. Shen, G. Luo, D. Li and D. Wang, *Chem. Eng. J.*, 2023, **478**, 147287.
14 X. Wang, L. Hu, K. C. Neyerlin and R. K. Ahluwalia, *J. Electrochem. Soc.*, 2023, **170**, 024503.
15 R. Ahluwalia, X. Wang, K. Chen, X. Wang and J. S. Spendelow, *J. Electrochem. Soc.*, 2024, **171**, 114512.
16 S. Cherevko, N. Kulyuk and K. J. J. Mayrhofer, *Nano Energy*, 2016, **29**, 275.
17 R. K. Ahluwalia, D. D. Papadias, N. N. Kariuki, J.-K. Peng, X. Wang, Y. Tsai, D. G. Graczyk and D. J. Myers, *J. Electrochem. Soc.*, 2018, **165**, F3024.
18 B. T. Sneed, D. A. Cullen, R. Mukundan, R. L. Borup and K. L. More, *J. Electrochem. Soc.*, 2018, **165**, F3078.
19 E. Padgett, V. Yarlagadda, M. E. Holtz, M. Ko, B. D. A. Levin, R. S. Kukreja, J. M. Ziegelbauer, R. N. Andrews, J. Ilavsky and A. Kongkanand, *J. Electrochem. Soc.*, 2019, **166**, F198.
20 K. Kodama, R. Jinnouchi, T. Suzuki, H. Murata, T. Hatanaka and Y. Morimoto, *Electrochem. Commun.*, 2013, **36**, 26.
21 K. Kodama, A. Shinohara, N. Hasegawa, K. Shinozaki, R. Jinnouchi, T. Suzuki, T. Hatanaka and Y. Morimoto, *J. Electrochem. Soc.*, 2014, **161**, F649.
22 N. Macauley, D. D. Papadias, J. Fairweather, D. Spernjak, D. Langlois, R. Ahluwalia, K. L. More, R. Mukundan and R. L. Borup, *J. Electrochem. Soc.*, 2018, **165**, F3148.
23 S. G. Ji, H. C. Kwon, T.-H. Kim, U. Sim and C. H. Choi, *ACS Catal.*, 2022, **12**, 7317.
24 H. Daimon, S. Yamazaki, M. Asahi, T. Ioroi and M. Inaba, *ACS Catal.*, 2022, **12**, 8976.
25 M. Chisaka, *J. Mater. Chem. A*, 2024, **12**, 18636.
26 R. Nishiizumi, T. Ogawa, K. Sanami, M. Yasutakea, Z. Noda, S. M. Lyth, M. Nishihara, J. Matsuda and K. Sasaki, *Int. J. Hydrogen Energy*, 2024, **72**, 820.
27 T. Toda, H. Igarashi, H. Uchida and M. Watanabe, *J. Electrochem. Soc.*, 1999, **146**, 3750.
28 K. Okaya, H. Yano, K. Kakinuma, M. Watanabe and H. Uchida, *ACS Appl. Mater. Interfaces*, 2012, **4**, 6982.
29 D. Wang, H. L. Xin, R. Hovden, H. Wang, Y. Yuauth-David, D. A. Muller, F. J. DiSalvo and H. D. Abruña, *Nat. Mater.*, 2013, **12**, 81.
30 Q. Jia, K. Caldwell, K. Strickland, J. M. Ziegelbauer, Z. Liu, Z. Yu, D. E. Ramaker and S. Mukerjee, *ACS Catal.*, 2015, **5**, 176.

31 W. S. Jung and B. N. Popov, *ACS Appl. Mater. Interfaces*, 2017, **9**, 23679.
32 A. Gunnarson, J. D. Bellis, T. Imhof, N. Pfänder, M. Ledendecker and F. Schüth, *Chem. Mater.*, 2023, **35**, 2006.
33 T. Takeguchi, T. Yamanaka, K. Asakura, E. N. Muhamad, K. Uosaki and W. Ueda, *J. Am. Chem. Soc.*, 2012, **134**, 14508.
34 R. Makharia, S. S. Kocha, P. T. Yu, M. A. Sweikart, W. Gu, F. T. Wagner and H. A. Gasteiger, *ECS Trans.*, 2006, **1**, 3.
35 Y. J. Wang, N. Zhao, B. Fang, H. Li, X. T. Bi and H. Wang, *Chem. Rev.*, 2015, **115**, 3433.
36 S. C. Zignani, E. Antolini and E. R. Gonzalez, *J. Power Sources*, 2008, **182**, 83.
37 K. Shinozaki, J. W. Zack, S. Pylypenko, B. S. Pivovar and S. S. Kocha, *J. Electrochem. Soc.*, 2015, **162**, F1384.
38 S. Treimer, A. Tang and D. C. Johnson, *Electroanalysis*, 2002, **14**, 165.
39 T. Nagai, C. Jahn and H. Jia, *J. Electrochem. Soc.*, 2019, **166**, F3111.
40 PEFC Evaluation Protocol from New Energy and Industrial Technology Development Organization (NEDO), 2023, **https://www.nedo.go.jp/content/100963953.pdf** and **https://www.fc-cubic.or.jp/en/pages/technical-info/**.
41 D. Kido, M. M. Rahman, T. Takeguchi and K. Asakura, *Chem. Lett.*, 2022, **51**, 538.
42 M. R. Z. Ghavidel and E. B. Easton, *Appl. Catal. B: Environ.*, 2015, **176–177**, 150.
43 P. Atkins, T. Overton, J. Rourke, M. Weller, F. Armstrong and M. Hagerman, *Shriver and Atkins' Inorganic Chemistry*, 5th edn, 2010, pp. 22–23.
44 J. F. Moulder, W. F. Stickle, P. E. Sobol and K. D. Bomben, Handbook of X-ray Photoelectron Spectroscopy: A Reference Book of Standard Spectra for Identification and Interpretation of XPS Data. 1992.
45 H. Li, K. Shin and G. Henkelman, *J. Chem. Phys.*, 2018, **149**, 174705.
46 P. Yu, M. Pemberton and P. Plasse, *J. Power Sources*, 2005, **144**, 11.
47 V. R. Stamenkovic, B. S. Mun, M. Arenz, K. J. J. Mayrhofer, C. A. Lucas, G. Wang, P. N. Ross and N. M. Markovic, *Nat. Mater.*, 2007, **6**, 241.
48 H. R. Colón-Mercado and B. N. Popov, *J. Power Sources*, 2006, **155**, 253.
49 L.-Y. Jiang, A.-J. Wang, X.-S. Li, J. Yuan and J.-J. Feng, *ChemElectroChem*, 2017, **4**, 2909.